

Supplemental Information

Supplemental methods

Study system

We considered “yellow pine/mixed-conifer forest” to be all areas designated as a yellow pine, dry mixed-conifer, or moist mixed-conifer pre-settlement fire regime (PFR) in the USFS Fire Return Interval Departure database (<https://www.fs.usda.gov/detail/r5/landmanagement/gis/?cid=STELPRDB5327836>), which reflects potential vegetation and is less sensitive to recent land cover change (Steel *et al.* 2018). We considered the Sierra Nevada region to be the area within the Sierra Nevada Foothills, the High Sierra Nevada, and the Tehachapi Mountain Area Jepson ecoregions (JepsonFloraProject 2016).

Remote sensing vegetation characteristics, including forest structural variability

Vegetation characteristics can be measured using remotely-sensed imagery (Rouse *et al.* 1973; Asner *et al.* 2016; Young *et al.* 2017) and texture analysis of this imagery can quantify ecologically relevant local environmental heterogeneity across broad spatial extents (Wood *et al.* 2012; Huang *et al.* 2014; Stein *et al.* 2014; Tuanmu & Jetz 2015; Graham *et al.* 2019), which may be used as a direct measure of ecosystem resilience (Kéfi *et al.* 2014). Developed for image classification and computer vision, texture analysis characterizes each pixel in an image by a summary statistic of its neighboring pixels, and represents a measure of local heterogeneity which itself varies across the landscape (Haralick *et al.* 1973). Texture analysis of forested areas detects heterogeneity of overstory vegetation, which corresponds to fuel loading and continuity, capturing the primary influence of vegetation structure on fire behavior.

Remote sensing potential annual heat load

We used the digital elevation model to calculate the potential annual heat load (Supplemental Equation 5 at each pixel, which is an integrated measure of latitude, slope, and a folding transformation of aspect about the northeast-southwest line, such that northeast becomes 0 radians and southwest becomes π radians (McCune & Keon 2002; with correction in McCune 2007):

$$\begin{aligned}
aspect_{folded} &= |\pi - |aspect - \frac{5\pi}{4}|| \\
&- 1.467 + \\
&1.582 * \cos(latitude) \cos(slope) - \\
(1) \quad log(pahl) &= 1.5 * \cos(aspect_{folded}) \sin(slope) \sin(latitude) - \\
&0.262 * \sin(lat) \sin(slope) + \\
&0.607 * \sin(aspect_{folded}) \sin(slope)
\end{aligned}$$

Where *pahl* is the potential annual heat load, *aspect_{folded}* is a transformation of aspect in radians, and both *latitude* and *slope* are extracted from a digital elevation model with units of radians.

Remote sensing wildfire severity

Wildfire severity typically describes the proportion of vegetation mortality resulting from fire (Keeley 2009), and can be measured by comparing pre- and postfire satellite imagery for a specific area (Key & Benson 2006). This usually requires considerable manual effort for image collation and processing, followed by calibration with field data (Miller & Thode 2007; Miller *et al.* 2009; De Santis *et al.* 2010; Cansler & McKenzie 2012; Veraverbeke & Hook 2013; Parks *et al.* 2014; Prichard & Kennedy 2014; Edwards *et al.* 2018; Fernández-García *et al.* 2018). Herculean efforts to measure severity across broad spatial extents, such as the Monitoring Trends in Burn Severity project (Eidenshink *et al.* 2007), exist but often must sacrifice coverage of smaller fires which are far more common (Calkin *et al.* 2005), may have different severity expectations compared to larger fires (Cansler & McKenzie 2014; Harvey *et al.* 2016), and are generally important contributors to global fire effects (Randerson *et al.* 2012). Automated efforts to remotely assess wildfire have arisen, but they tend to focus on more aggregate measures of wildfire such as whether an area burned or the probability that it burned rather than the severity of the burn (Bastarrika *et al.* 2011; Goodwin & Collett 2014; Boschetti *et al.* 2015; Hawbaker *et al.* 2017), but see (Reilly *et al.* 2017; Parks *et al.* 2018a). Here, we present a method to automate the measurement of wildfire severity using minimal user inputs: a geometry of interest (a wildfire perimeter or a field plot location) and an alarm date (the date the fire was discovered). This information is readily available in many fire-prone areas (such as California, via the Fire and Resource Assessment Program; <https://frap.fire.ca.gov/frap-projects/fire-perimeters/>) or could be derived using existing products (such as the Landsat Burned Area Essential Climate Variable product described in Hawbaker *et al.* (2017)).

We calibrate 28 configurations of our algorithmic approach to ground-based wildfire severity measurements, and select the best performing severity metric to generate a comprehensive, system-wide severity dataset. Our

approach more than doubles the number of fire events represented from 432 to 1008, though only increases the total burned area represented from $7.40\text{e}+05$ to $8.27\text{e}+05$ hectares because most of the additional fires are small.

Fetching and processing pre- and postfire imagery

For each fire perimeter, we fetched a time series of prefire Landsat images starting the day before the fire alarm date and extending backward in time by a pre-defined time window. An analogous postfire time series of Landsat imagery was fetched exactly one year after the date range used to filter the prefire collection. We tested 4 time windows, 16, 32, 48, or 64 days, which were chosen to ensure that at least 1, 2, 3, or 4 Landsat images were captured by the date range (Supplemental Fig. 1). The Landsat archive we filtered included imagery from Landsat 4, 5, 7, and 8, so each pre- and postfire image collection may contain a mix of scenes from different satellite sources to enhance coverage. For each image in the pre- and postfire image collections, we masked pixels that were not clear (i.e., clouds, cloud shadows, snow, and water) using the CFMask algorithm (Foga *et al.* 2017).

For each Landsat image in the prefire and postfire collections, we calculated standard indices that capture vegetation cover and fire effects such as charring. Normalized difference vegetation index (NDVI) correlates with vegetation density, canopy cover, and leaf area index (Rouse *et al.* 1973). Normalized burn ratio (NBR) and normalized burn ratio version 2 (NBR2) respond strongly to fire effects on vegetation (García & Caselles 1991; Key & Benson 2006; Hawbaker *et al.* 2017; USGS 2017a, b) (Equations in Supplemental Methods).

We composited each pre- and postfire image collection (including the pixel values representing NDVI, NBR, and NBR2) into a single pre- and postfire image using a median reducer, which calculated the median of the unmasked values on a per-pixel basis across the stack of images in each collection. Composite pre- and postfire images can be successfully used to measure wildfire severity instead of using raw, individual images (Parks *et al.* 2018a, 2019).

Spectral indices of wildfire severity

Using the composited images, we calculated commonly used metrics of remotely-sensed wildfire severity to validate against ground-based data: the relative burn ratio (RBR) (Parks *et al.* 2014), the delta normalized burn ratio (dNBR) (Eidenshink *et al.* 2007; Miller & Thode 2007), the relative delta normalized burn ratio (RdNBR) (Miller & Thode 2007; Miller & Safford 2012), the delta normalized burn ratio 2 (dNBR2) (Hawbaker *et al.* 2017), the relative delta normalized burn ratio 2 (RdNBR2), and the delta normalized difference vegetation index (dNDVI) (Eidenshink *et al.* 2007). We also calculated an analogous metric to

RdNBR using NDVI: the relative delta normalized difference vegetation index (RdNDVI). Following Reilly *et al.* (2017), we did not correct the delta indices using a phenological offset value, as our approach implicitly accounts for phenology by incorporating multiple cloud-free images across the same time window both before the fire and one year later.

Normalized difference vegetation index (NDVI; Supplemental Equation 1) correlates with vegetation density, canopy cover, and leaf area index (Rouse *et al.* 1973). Normalized burn ratio (NBR; Supplemental Equation 3) and normalized burn ratio version 2 (NBR2; Supplemental Equation 4) respond strongly to fire effects on vegetation (García & Caselles 1991; Key & Benson 2006; Hawbaker *et al.* 2017; USGS 2017b, a).

$$(2) \ ndvi = (nir - red) / (nir + red) * 1000$$

$$(3) \ nbr = (nir - swir2) / (nir + swir2) * 1000$$

$$(4) \ nbr2 = (swir1 - swir2) / (swir1 + swir2) * 1000$$

Where *nir* is the near infrared band (band 4 on Landsat 4, 5, and 7; band 5 on Landsat 8) and *red* is the red band (band 3 on Landsat 4, 5, and 7; band 4 on Landsat 8), *swir1* is the first short wave infrared band (band 5 on Landsat 4, 5, and 7; band 4 on Landsat 8), *swir2* is the second short wave infrared band (band 7 on Landsat 4, 5, 7, and 8)

We calculated the delta severity indices (dNBR, dNBR2, dNDVI) by subtracting the respective postfire indices from the prefire indices (NBR, NBR2, and NDVI) without multiplying by a rescaling constant (e.g., we did not multiply the result by 1000 as in Miller & Thode (2007); Supplemental Equation 6). Following Reilly *et al.* (2017), we chose not to correct the delta indices using a phenological offset value (typically calculated as the delta index in homogeneous forest patch outside of the fire perimeter), as our approach implicitly accounts for phenology by incorporating multiple cloud-free images across the same time window both before the fire and one year later.

$$(5) \ dI = I_{\text{prefire}} - I_{\text{postfire}}$$

We calculated the relative delta severity indices, RdNBR and RdNDVI, by scaling the respective delta indices (dNBR and dNDVI) from Supplemental Equation 7 by a square root transformation of the absolute value of the prefire index:

$$(6) \ RdI = \frac{dI}{\sqrt{|I_{\text{prefire}}|/1000}}$$

We calculated the relative burn ratio (RBR) following Parks *et al.* (2014) using Supplemental Equation 8:

$$(7) \ RBR = \frac{dNBR}{NBR_{\text{prefire}}/1000+1.001}$$

Calibrating remotely-sensed wildfire severity with field-measured wildfire severity

We calibrated these 28 severity metrics with 208 field measures of fire effects to overstory vegetation—the overstory component of the Composite Burn Index (CBI)—from two previously published studies (Zhu *et al.* 2006; Sikkink *et al.* 2013). CBI is a metric of vegetation mortality across several vertical vegetation strata within a 30m diameter field plot, and the overstory component characterizes fire effects to the overstory vegetation specifically (Key & Benson 2006). CBI ranges from 0 (no fire impacts) to 3 (very high fire impacts), and has a long and successful history of use as a standard for calibrating remotely-sensed severity data in western U.S. dry forests (Key & Benson 2006; Miller & Thode 2007; Miller *et al.* 2009; Cansler & McKenzie 2012; Parks *et al.* 2014, 2018a; Prichard & Kennedy 2014).

Following Miller & Thode (2007), Miller *et al.* (2009), Parks *et al.* (2014), and Parks *et al.* (2018a), we fit a non-linear model to each remotely-sensed severity metric of the following form:

$$(8) \text{ remote_severity} = \beta_0 + \beta_1 e^{\beta_2 \text{cbi_overstory}}$$

We fit the model in Supplemental Equation 9 for all 7 of our remotely-sensed severity metrics (RBR, dNBR, RdNBR, dNBR2, RdNBR2, dNDVI, RdNDVI) using 4 different time windows from which to collate satellite imagery (16, 32, 48, and 64 days). Following Cansler & McKenzie (2012), Parks *et al.* (2014), and Parks *et al.* (2018a), we used bilinear interpolation to extract remotely-sensed severity at the locations of the CBI field plots to better align remote and field measurements. We also extracted remotely-sensed severity values using bicubic interpolation, which produces smoother imagery but is more computationally demanding. In total, we fit 56 models (7 severity measures, 4 time windows, 2 interpolation methods) and performed five-fold cross validation using the `modelr` and `purrr` packages in R (R Core Team 2018; Henry & Wickham 2019; Wickham 2019). To compare goodness of model fits with Miller & Thode (2007), Miller *et al.* (2009), and Parks *et al.* (2014), we report the average R^2 value from the cross validation for each of the 56 models.

Some implications of this methodological development

We developed an approach to calculating wildfire severity leveraging the cloud-based data catalog, the large parallel processing system, and the distribution of computation tasks in Google Earth Engine to enable rapid high-throughput analyses of earth observation data (Gorelick *et al.* 2017; Parks *et al.* 2018b, 2019). Our programmatic assessment of wildfire severity across the 1008 Sierra Nevada yellow pine/mixed-conifer fires in the FRAP perimeter database, which enabled consistent assessment of severity for a broad representation of fires including smaller events (Randerson *et al.* 2012). We found that the relative burn ratio (RBR) calculated using prefire Landsat images collected over a 48-day period prior to the fire and postfire Landsat images

collected over a 48-day period one year after the prefire images validated the best with ground-based severity measurements (composite burn index; CBI). Further, we found that this programmatic approach was robust to a wide range of severity metrics, time windows, and interpolation techniques.

We echo the conclusion of Zhu *et al.* (2006) that the validation of differences between pre- and postfire NDVI to field-measured severity data, which uses near infrared reflectance, is comparable to validation using more commonly used severity metrics (e.g., RdNBR and RBR) that rely on short wave infrared reflectance. One immediately operational implication of this is that the increasing availability of low-cost small unhumanned aerial systems (sUAS a.k.a. drones) and near-infrared-detecting imagers (e.g., those used for agriculture monitoring) may be used to reliably assess wildfire severity at very high spatial resolutions.

Supplemental figures and tables

Supplemental Table 1: Comparison of models used to validate and calibrate remotely sensed wildfire severity with ground-based composite burn index (CBI) severity sorted in descending order by the R^2 value from a 10-fold cross validation. A total of 56 models were tested representing all possible combinations of 7 different measures of wildfire severity (RBR, dNBR, dNBR2, RdNBR, RdNBR2, dNDVI, and RdNDVI), 4 different time windows in which Landsat imagery was acquired and summarized with a median reducer on a pixel-by-pixel basis (16 days, 32 days, 48 days, and 64 days), and two different interpolation methods (bilinear and bicubic). The three parameters (β_0 , β_1 , and β_2) from the nonlinear model fit described in Eq. 1 are reported. For each model, the value of the remotely sensed wildfire severity measurement corresponding to the lower bounds of 3 commonly used categories of severity are reported ('low' corresponds to a CBI value of 0.1, 'mod' corresponds to a CBI value of 1.25, and 'high' corresponds to a CBI value of 2.25)

Rank	Severity	Time	k-fold							
	measure	window	Interpolation	R^2	β_0	β_1	β_2	low	mod	high
1	RBR	48	bicubic	0.806	13.88	28.24	1.001	45.1	112.6	282.3
2	RdNBR	32	bilinear	0.802	-15.28	96.81	0.857	90.19	267.2	650.1
3	RdNDVI	32	bilinear	0.802	-80.04	100.4	0.624	26.85	138.9	328.5
4	RBR	64	bilinear	0.796	17.08	27.37	1.003	47.34	113	278.7
5	RdNDVI	48	bicubic	0.796	-82.95	114.6	0.587	38.58	155.7	346.1
6	RdNDVI	64	bicubic	0.793	-79.8	112.9	0.59	39.94	156.1	345.6
7	RdNBR	64	bilinear	0.791	-13.29	95.85	0.862	91.19	268.3	653.4
8	RdNDVI	32	bicubic	0.789	-86.56	104.6	0.619	24.74	140.3	334.7
9	RdNBR	48	bicubic	0.787	-27.14	101.8	0.852	83.7	268	664.7
10	RdNDVI	48	bilinear	0.785	-67.8	103.5	0.609	42.21	153.9	340
11	RBR	32	bicubic	0.785	13.38	28.94	0.994	45.34	113.6	284
12	RdNDVI	64	bilinear	0.778	-67.67	103.9	0.607	42.77	154.2	339.3

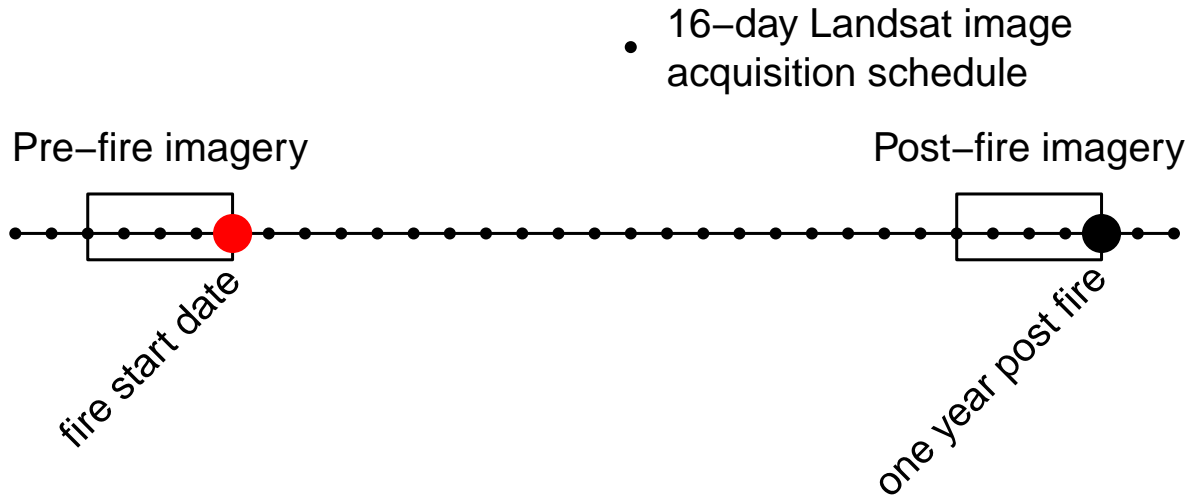
Rank	Severity	Time	k-fold							
	measure	window	Interpolation	R^2	β_0	β_1	β_2	low	mod	high
13	RBR	32	bilinear	0.773	14.45	28.92	0.985	46.35	113.5	279.6
14	RBR	64	bicubic	0.772	15.62	27.48	1.01	46.02	112.8	282.5
15	dNDVI	32	bicubic	0.766	-57.93	72.92	0.65	19.89	106.4	257
16	RdNBR	32	bicubic	0.765	-30.17	105.6	0.841	84.72	272	670.4
17	RdNBR	16	bicubic	0.763	11.69	77.35	0.926	96.55	257.7	632.4
18	RBR	48	bilinear	0.762	17.4	27.02	1.006	47.28	112.4	277.4
19	dNDVI	32	bilinear	0.76	-52.76	69.58	0.656	21.53	105.2	251.8
20	dNBR	16	bicubic	0.76	31.67	36.21	1.058	71.92	167.6	423.1
21	dNBR	32	bilinear	0.756	29.08	36.05	1.048	69.12	162.7	409.9
22	dNBR	48	bicubic	0.753	29.81	34.55	1.069	68.25	161.3	413
23	dNDVI	64	bilinear	0.75	-46.03	74.88	0.627	33.69	117.9	261
24	RdNBR	64	bicubic	0.749	-45.8	115.5	0.819	79.53	275.7	683.4
25	RdNBR2	64	bilinear	0.746	64.09	14.28	1.204	80.2	128.4	278.3
26	RBR	16	bilinear	0.741	21.28	26.04	1.016	50.1	114	277.6
27	RBR	16	bicubic	0.741	20.64	25.8	1.028	49.24	113.9	281.4
28	dNBR	64	bicubic	0.741	33.09	32.97	1.086	69.84	161.2	412.7
29	RdNBR2	32	bicubic	0.74	45.08	18.99	1.125	66.33	122.6	283.8
30	RdNBR2	48	bilinear	0.738	56.99	15.7	1.174	74.65	125.1	277.2
31	dNDVI	48	bilinear	0.733	-43.97	72.96	0.637	33.79	117.9	262.1
32	RdNDVI	16	bicubic	0.731	-39.46	84.78	0.665	51.16	155.2	339
33	RdNBR2	48	bicubic	0.729	58.02	14.54	1.209	74.43	123.9	278.9
34	RdNBR	16	bilinear	0.728	8.831	79.63	0.909	96.04	256.7	623.8
35	dNDVI	48	bicubic	0.725	-55.06	81.08	0.613	31.15	119.4	266.9
36	dNDVI	64	bicubic	0.721	-55.2	81.59	0.609	31.51	119.5	266.1
37	dNBR2	32	bilinear	0.72	25.56	8.591	1.149	35.2	61.7	139.6
38	dNBR2	32	bicubic	0.72	25.41	8.256	1.177	34.7	61.35	142
39	dNBR	32	bicubic	0.719	27.74	36.12	1.057	67.89	163.2	417.5
40	dNBR	48	bilinear	0.718	34.76	32.84	1.076	71.33	160.9	404.8
41	RdNDVI	16	bilinear	0.709	-31.08	79.15	0.678	53.61	153.5	332.5
42	RdNBR2	32	bilinear	0.705	45.37	19.76	1.1	67.42	123.5	280.2

Rank	Severity	Time	k-fold							
	measure	window	Interpolation	R^2	β_0	β_1	β_2	low	mod	high
43	dNBR	16	bilinear	0.703	32.68	36.36	1.048	73.05	167.3	416.5
44	dNBR2	48	bilinear	0.7	32.6	6.298	1.248	39.74	62.56	136.9
45	dNBR2	48	bicubic	0.698	33.08	5.838	1.284	39.72	62.15	138
46	dNBR2	64	bicubic	0.689	37.2	5.289	1.313	43.23	64.48	138.6
47	RdNBR2	64	bicubic	0.688	66.47	13.14	1.24	81.35	128.4	280.2
48	dNDVI	16	bilinear	0.671	-23.13	60.35	0.689	41.52	119.6	261.1
49	dNDVI	16	bicubic	0.659	-29.98	65.13	0.674	39.69	121.2	266.5
50	RdNBR	48	bilinear	0.658	-108.9	162.3	0.724	65.53	292	717.8
51	dNBR	64	bilinear	0.654	35.08	32.67	1.08	71.48	161.1	406.1
52	dNBR2	64	bilinear	0.639	36.14	5.641	1.283	42.55	64.17	137.2
53	RdNBR2	16	bicubic	0.638	59.17	14.77	1.198	75.83	125.2	278
54	RdNBR2	16	bilinear	0.622	60.98	14.69	1.189	77.53	125.9	274.4
55	dNBR2	16	bilinear	0.611	29.84	8.754	1.138	39.65	66.17	143.2
56	dNBR2	16	bicubic	0.562	29.49	8.601	1.156	39.15	65.95	145.3

Supplemental Table 2: Model parameter estimates for different neighborhood sizes. Values represent the mean parameter estimates with 95% credible intervals in parentheses.

Coefficient	90 x 90m	150 x 150m	210 x 210m	270 x 270m
	neighborhood	neighborhood	neighborhood	neighborhood
β_0	-2.414 (-2.575, -2.258)	-2.43 (-2.589, -2.275)	-2.435 (-2.598, -2.28)	-2.444 (-2.598, -2.29)
$\beta_{nbhd_stdev_NDVI}$	-0.213 (-0.251, -0.174)	-0.219 (-0.259, -0.177)	-0.211 (-0.254, -0.167)	-0.202 (-0.246, -0.157)
$\beta_{prefire_NDVI}$	1.06 (0.931, 1.192)	1.139 (1.041, 1.236)	1.143 (1.059, 1.226)	1.126 (1.052, 1.201)
β_{fm100}	-0.576 (-0.709, -0.442)	-0.573 (-0.717, -0.434)	-0.57 (-0.707, -0.438)	-0.573 (-0.715, -0.439)
β_{pahl}	0.246 (0.215, 0.277)	0.244 (0.213, 0.275)	0.245 (0.215, 0.276)	0.246 (0.216, 0.277)

	90 x 90m	150 x 150m	210 x 210m	270 x 270m
Coefficient	neighborhood	neighborhood	neighborhood	neighborhood
$\beta_{\text{topographic_roughness}}$	0.002 (-0.029, 0.034)	0.007 (-0.026, 0.039)	0.01 (-0.022, 0.043)	0.011 (-0.023, 0.046)
$\beta_{\text{nbhd_mean_NDVI}}$	-0.168 (-0.311, -0.028)	-0.289 (-0.398, -0.182)	-0.308 (-0.406, -0.21)	-0.298 (-0.388, -0.207)
$\beta_{\text{nbhd_stdev_NDVI*prefire_NDVI}}$	0.128 (0.031, 0.221)	0.062 (-0.011, 0.135)	0.028 (-0.037, 0.092)	0.016 (-0.045, 0.078)
$\beta_{\text{nbhd_stdev_NDVI*nbhd_mean_NDVI}}$	-0.115 (-0.206, -0.022)	-0.057 (-0.13, 0.014)	-0.012 (-0.074, 0.05)	0.01 (-0.048, 0.068)
$\beta_{\text{nbhd_stdev_NDVI*fm100}}$	-0.032 (-0.073, 0.01)	-0.028 (-0.072, 0.016)	-0.02 (-0.065, 0.024)	-0.01 (-0.056, 0.036)
$\beta_{\text{nbhd_mean_NDVI*prefire_NDVI}}$	-0.54 (-0.587, -0.494)	-0.53 (-0.577, -0.483)	-0.517 (-0.565, -0.47)	-0.505 (-0.552, -0.458)



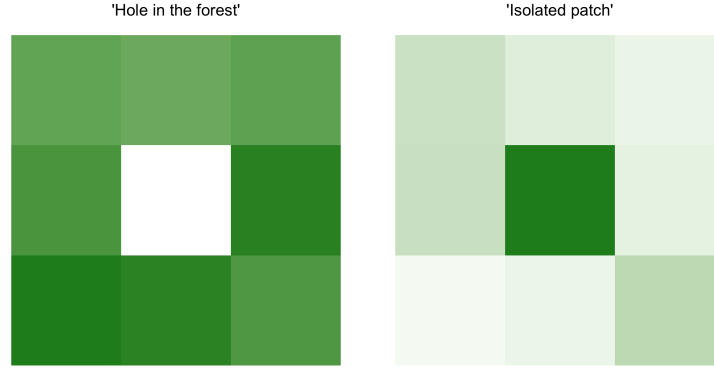
Supplemental Figure 1: Schematic for how Landsat imagery was assembled in order to make comparisons between pre- and post-fire conditions. This schematic depicts a 64-day window of image collation prior to the fire which comprise the pre-fire image collection. A similar, 64-day window collection of imagery is assembled one year after the pre-fire image collection.

Data availability

All data and analysis code are available via the Open Science Framework (DOI: 10.17605/OSF.IO/27NSR) including a new dataset representing wildfire severity, vegetation characteristics, and regional climate conditions within the perimeters of 1,090 fires from the FRAP database that burned in yellow pine/mixed-conifer forest in the Sierra Nevada, California between 1984 and 2018.

References

1.
Asner, G.P., Brodrick, P.G., Anderson, C.B., Vaughn, N., Knapp, D.E. & Martin, R.E. (2016). Progressive forest canopy water loss during the 2012-2015 California drought. *Proceedings of the National Academy of Sciences*, 113, E249–E255.
2.
Bastarrika, A., Chuvieco, E. & Martín, M.P. (2011). Mapping burned areas from Landsat TM/ETM+ data with a two-phase algorithm: Balancing omission and commission errors. *Remote Sensing of Environment*, 115, 1003–1012.
- 3.



Supplemental Figure 2: Conceptual diagram of ‘decoupling’ that sometimes occurs between the central pixel NDVI and the neighborhood mean NDVI. In each of these scenarios, our model results suggest that the probability that the central pixel burns at high severity is higher than expected given the additive effect of the covariates. The left panel depicts the “hole in the forest” decoupling, which occurs more frequently, and the right panel depicts the “isolated patch” decoupling.

Boschetti, L., Roy, D.P., Justice, C.O. & Humber, M.L. (2015). MODISLandsat fusion for large area 30m burned area mapping. *Remote Sensing of Environment*, 161, 27–42.

4.

Calkin, D.E., Gebert, K.M., Jones, J.G. & Neilson, R.P. (2005). Forest Service large fire area burned and suppression expenditure trends, 19702002. *J for*, 103, 179–183.

5.

Cansler, C.A. & McKenzie, D. (2012). How robust are burn severity indices when applied in a new region? Evaluation of alternate field-based and remote-sensing methods. *Remote Sensing*, 4, 456–483.

6.

Cansler, C.A. & McKenzie, D. (2014). Climate, fire size, and biophysical setting control fire severity and spatial pattern in the northern Cascade Range, USA. *Ecological Applications*, 24, 1037–1056.

7.

De Santis, A., Asner, G.P., Vaughan, P.J. & Knapp, D.E. (2010). Mapping burn severity and burning efficiency in California using simulation models and Landsat imagery. *Remote Sensing of Environment*, 114, 1535–1545.

8.

Edwards, A.C., Russell-Smith, J. & Maier, S.W. (2018). A comparison and validation of satellite-derived fire severity mapping techniques in fire prone north Australian savannas: Extreme fires and tree stem mortality. *Remote Sensing of Environment*, 206, 287–299.

- 183 9.
- 184 Eidenshink, J., Schwind, B., Brewer, K., Zhu, Z.-L., Quayle, B. & Howard, S. (2007). A project for monitoring
185 trends in burn severity. *Fire Ecology*, 3, 3–21.
- 186 10.
- 187 Fernández-García, V., Santamarta, M., Fernández-Manso, A., Quintano, C., Marcos, E. & Calvo, L. (2018).
188 Burn severity metrics in fire-prone pine ecosystems along a climatic gradient using Landsat imagery. *Remote*
189 *Sensing of Environment*, 206, 205–217.
- 190 11.
- 191 Foga, S., Scaramuzza, P.L., Guo, S., Zhu, Z., Dilley, R.D. & Beckmann, T. *et al.* (2017). Cloud detection
192 algorithm comparison and validation for operational Landsat data products. *Remote Sensing of Environment*,
193 194, 379–390.
- 194 12.
- 195 García, M.L. & Caselles, V. (1991). Mapping burns and natural reforestation using thematic Mapper data.
196 *Geocarto International*, 6, 31–37.
- 197 13.
- 198 Goodwin, N.R. & Collett, L.J. (2014). Development of an automated method for mapping fire history captured
199 in Landsat TM and ETM+ time series across Queensland, Australia. *Remote Sensing of Environment*, 148,
200 206–221.
- 201 14.
- 202 Gorelick, N., Hancher, M., Dixon, M., Ilyushchenko, S., Thau, D. & Moore, R. (2017). Google Earth Engine:
203 Planetary-scale geospatial analysis for everyone. *Remote Sensing of Environment*, 202, 18–27.
- 204 15.
- 205 Graham, L.J., Spake, R., Gillings, S., Watts, K. & Eigenbrod, F. (2019). Incorporating fine-scale environmental
206 heterogeneity into broad-extent models. *Methods in Ecology and Evolution*, 10, 767–778.
- 207 16.
- 208 Haralick, R.M., Shanmugam, K. & Dinstein, I. (1973). Textural features for image classification. *IEEE*
209 *Transactions on Systems, Man, and Cybernetics*, SMC-3, 610–621.
- 210 17.
- 211 Harvey, B.J., Donato, D.C. & Turner, M.G. (2016). Drivers and trends in landscape patterns of stand-replacing
212 fire in forests of the US Northern Rocky Mountains (1984-2010). *Landscape Ecology*, 31, 2367–2383.

18.

Hawbaker, T.J., Vanderhoof, M.K., Beal, Y.-J., Takacs, J.D., Schmidt, G.L. & Falgout, J.T. *et al.* (2017). Mapping burned areas using dense time-series of Landsat data. *Remote Sensing of Environment*, 198, 504–522.

19.

Henry, L. & Wickham, H. (2019). *Purrr: Functional programming tools*.

20.

Huang, Q., Swatantran, A., Dubayah, R. & Goetz, S.J. (2014). The influence of vegetation height heterogeneity on forest and woodland bird species richness across the United States. *PLoS ONE*, 9, e103236.

21.

JepsonFloraProject (Ed.). (2016). *Jepson eFlora*.

22.

Keeley, J.E. (2009). Fire intensity, fire severity and burn severity: A brief review and suggested usage. *International Journal of Wildland Fire*, 18, 116.

23.

Key, C.H. & Benson, N.C. (2006). Landscape assessment (LA): Sampling and analysis methods, 55.

24.

Kéfi, S., Guttal, V., Brock, W.A., Carpenter, S.R., Ellison, A.M. & Livina, V.N. *et al.* (2014). Early warning signals of ecological transitions: Methods for spatial patterns. *PLoS ONE*, 9, e92097.

25.

McCune, B. (2007). Improved estimates of incident radiation and heat load using non- parametric regression against topographic variables. *Journal of Vegetation Science*, 18, 751–754.

26.

McCune, B. & Keon, D. (2002). Equations for potential annual direct incident radiation and heat load. *Journal of Vegetation Science*, 13, 603–606.

27.

Miller, J.D., Knapp, E.E., Key, C.H., Skinner, C.N., Isbell, C.J. & Creasy, R.M. *et al.* (2009). Calibration and validation of the relative differenced Normalized Burn Ratio (RdNBR) to three measures of fire severity in the Sierra Nevada and Klamath Mountains, California, USA. *Remote Sensing of Environment*, 113, 645–656.

28.

Miller, J.D. & Safford, H. (2012). Trends in wildfire severity: 1984 to 2010 in the Sierra Nevada, Modoc

243 Plateau, and Southern Cascades, California, U.S.A. *Fire Ecology*, 8, 41–57.

244 29.

245 Miller, J.D. & Thode, A.E. (2007). Quantifying burn severity in a heterogeneous landscape with a relative
 246 version of the delta Normalized Burn Ratio (dNBR). *Remote Sensing of Environment*, 109, 66–80.

247 30.

248 Parks, S.A., Holsinger, L.M., Koontz, M.J., Collins, L., Whitman, E. & Parisien, M.-A. *et al.* (2019). Giving
 249 ecological meaning to satellite-derived fire severity metrics across North American forests. *Remote Sensing*,
 250 11, 1735.

251 31.

252 Parks, S.A., Holsinger, L.M., Panunto, M.H., Jolly, W.M., Dobrowski, S.Z. & Dillon, G.K. (2018a). High-
 253 severity fire: Evaluating its key drivers and mapping its probability across western U.S. Forests. *Environmental*
 254 *Research Letters*, 13, 044037.

255 32.

256 Parks, S., Dillon, G. & Miller, C. (2014). A new metric for quantifying burn severity: The Relativized Burn
 257 Ratio. *Remote Sensing*, 6, 1827–1844.

258 33.

259 Parks, S., Holsinger, L., Voss, M., Loehman, R. & Robinson, N. (2018b). Mean composite fire severity metrics
 260 computed with Google Earth Engine offer improved accuracy and expanded mapping potential. *Remote*
 261 *Sensing*, 10, 879.

262 34.

263 Prichard, S.J. & Kennedy, M.C. (2014). Fuel treatments and landform modify landscape patterns of burn
 264 severity in an extreme fire event. *Ecological Applications*, 24, 571–590.

265 35.

266 Randerson, J.T., Chen, Y., Werf, G.R. van der, Rogers, B.M. & Morton, D.C. (2012). Global burned area
 267 and biomass burning emissions from small fires. *Journal of Geophysical Research: Biogeosciences*, 117.

268 36.

269 R Core Team. (2018). *R: A language and environment for statistical computing*. R Foundation for Statistical
 270 Computing, Vienna, Austria.

271 37.

272 Reilly, M.J., Dunn, C.J., Meigs, G.W., Spies, T.A., Kennedy, R.E. & Bailey, J.D. *et al.* (2017). Contemporary

273 patterns of fire extent and severity in forests of the Pacific Northwest, USA (1985-2010). *Ecosphere*, 8, e01695.

274 38.

275 Rouse, W., Haas, R.H., Deering, W. & Schell, J.A. (1973). *Monitoring the vernal advancement and*
 276 *retrogradation (green wave effect) of natural vegetation* (Type II Report No. RSC 1978-2). Goddard Space
 277 Flight Center, Greenbelt, MD, USA.

278 39.

279 Sikkink, P.G., Dillon, G.K., Keane, R.E., Morgan, P., Karau, E.C. & Holden, Z.A. *et al.* (2013). Composite
 280 Burn Index (CBI) data and field photos collected for the FIRESEV project, western United States.

281 40.

282 Steel, Z.L., Koontz, M.J. & Safford, H.D. (2018). The changing landscape of wildfire: Burn pattern trends
 283 and implications for California’s yellow pine and mixed conifer forests. *Landscape Ecology*, 33, 1159–1176.

284 41.

285 Stein, A., Gerstner, K. & Kreft, H. (2014). Environmental heterogeneity as a universal driver of species
 286 richness across taxa, biomes and spatial scales. *Ecology Letters*, 17, 866–880.

287 42.

288 Tuanmu, M.-N. & Jetz, W. (2015). A global, remote sensing-based characterization of terrestrial habitat
 289 heterogeneity for biodiversity and ecosystem modelling: Global habitat heterogeneity. *Global Ecology and*
 290 *Biogeography*, 24, 1329–1339.

291 43.

292 USGS. (2017a). Landsat 4-7 Surface Reflectance (LEDAPS) Product Guide, 41.

293 44.

294 USGS. (2017b). Landsat 8 Surface Reflectance Code (LASRC) Product Guide, 40.

295 45.

296 Veraverbeke, S. & Hook, S.J. (2013). Evaluating spectral indices and spectral mixture analysis for assessing
 297 fire severity, combustion completeness and carbon emissions. *International Journal of Wildland Fire*, 22, 707.

298 46.

299 Wickham, H. (2019). *Modelr: Modelling functions that work with the pipe*.

300 47.

301 Wood, E.M., Pidgeon, A.M., Radeloff, V.C. & Keuler, N.S. (2012). Image texture as a remotely sensed
 302 measure of vegetation structure. *Remote Sensing of Environment*, 121, 516–526.

303 48.

304 Young, D.J.N., Stevens, J.T., Earles, J.M., Moore, J., Ellis, A. & Jirka, A.L. *et al.* (2017). Long-term climate
305 and competition explain forest mortality patterns under extreme drought. *Ecology Letters*, 20, 78–86.

306 49.

307 Zhu, Z., Key, C., Ohlen, D. & Benson, N. (2006). *Evaluate sensitivities of burn-severity mapping algorithms*
308 *for different ecosystems and fire histories in the United States* (Final Report to the Joint Fire Science Program
309 No. JFSP 01-1-4-12).